

# Hydrogen Embrittlement Behavior of 430 and 445NF Ferritic Stainless Steels

SUN MI KIM, YOUNG SOO CHUN, SUNG YEUN WON, YOUNG HWAN KIM,  
and CHONG SOO LEE

Hydrogen embrittlement behavior of two kinds of commercial ferritic stainless steels (STSs), 430 (UNS S43000) and 445NF (UNS S44536), was investigated by means of a series of cathodical hydrogen charging, slow strain rate tests, bending tests, and thermal desorption spectrometry analyses. The hydrogen concentration in 445NF STS was lower than that of 430 STS under identical hydrogen charging conditions because of the formation of a more passive layer. In addition, 445NF STS exhibited a larger passive range in the potentiodynamic polarization curve. However, resistance to hydrogen embrittlement of 445NF STS was inferior to that of 430 STS because of precipitation of the Laves phase at grain boundaries of the former at annealing temperatures of 873 K to 1123 K (600 °C to 850 °C). Crack propagation was found to occur along the interface between the Laves phase and the matrix. For 445NF STS, dissolution of the Laves phase by solution heat treatment at 1273 K (1000 °C) followed by quenching was effective in terms of suppressing degradation of its mechanical properties and formability, which were related to hydrogen embrittlement.

DOI: 10.1007/s11661-012-1265-7

© The Minerals, Metals & Materials Society and ASM International 2012

## I. INTRODUCTION

STAINLESS steels (STSs) are widely used for both low-end applications, such as cooking utensils and furniture, and very sophisticated applications, such as space vehicles and construction materials, because of their desirable combinations of mechanical properties and corrosion resistance.<sup>[1]</sup> There are three main types of microstructures in STSs, *i.e.*, ferritic, austenitic, and martensitic. These microstructures can be obtained by properly adjusting the steel chemistry.

In the STS-related fields, many efforts have recently been devoted to replacing austenitic STSs with ferritic STSs. This is primarily because ferritic STSs have higher yield strength and superior stress corrosion cracking resistance compared to austenitic STSs.<sup>[1,2]</sup> In addition, the price of Ni, a major alloying element of austenitic STSs, is unstable and high. However, there are some drawbacks of ferritic STSs for replacement of austenitic STSs. One main drawback is their susceptibility to hydrogen embrittlement. Hydrogen absorbed from the environment during processing or service can cause

sudden failure<sup>[3]</sup> especially at regions of high stress concentration.<sup>[4-6]</sup> In general, hydrogen embrittlement resistance of body-centered cubic (bcc) structured ferrite is inherently inferior to that of face-centered cubic (fcc) structured austenite. Yu and Perng<sup>[7]</sup> measured that the hydrogen diffusivity in ferrite to be approximately 100,000 times higher than that in austenite at room temperature. Moreover, the solubility of hydrogen affects the hydrogen embrittlement resistance. Singh and Altstetter<sup>[5]</sup> reported that the austenitic steels have higher hydrogen solubility, by a factor of  $10^3$ . In ferritic steels, excessive hydrogen is trapped by structural defects, such as grain boundaries, dislocations and microvoids.<sup>[8]</sup> Trapped hydrogen atoms recombine as hydrogen molecule gas, and fracture is accelerated by various hydrogen embrittlement mechanisms.<sup>[9-12]</sup> Hydrogen also affects the surface quality of ferritic STSs. Szummer *et al.*<sup>[13]</sup> reported that hydrogen charging of ferritic STSs in an aqueous solution resulted in the formation of grain-oriented needle-shaped twins at the surface layer, and many microcracks formed inside such needle-shaped twins and conferred an embrittlement of the hydrogen charged materials.

445NF STS (UNS S44536) is a newly developed ferritic STS grade. Compared with conventional 430 ferritic STS (UNS S43000), it contains higher Nb and Ti contents to enhance mechanical properties such as durability and formability, as well as higher Cr content to improve the corrosion resistance. However, its application is limited by its ill-defined hydrogen embrittlement properties. In the current investigation, the hydrogen embrittlement behavior of 445NF STS was (1) examined by means of a series of cathodical hydrogen charging and slow strain rate tests and (2) compared with that of conventional 430 STS. In addition, the factors influencing hydrogen embrittlement of 445NF

---

SUN MI KIM and YOUNG SOO CHUN, Ph.D. Candidates, are with the Department of Materials Science and Engineering, Pohang University of Science and Technology, Pohang 790-784, Korea. SUNG YEUN WON, Ph.D. Senior Researcher, and YOUNG HWAN KIM, Ph.D. Senior Researcher and Group Leader, are with the Technical Research Laboratories, POSCO, Pohang 790-785, Korea. CHONG SOO LEE, Ph.D. Professor, is with the Department of Materials Science and Engineering, Pohang University of Science and Technology, and also with the Graduate Institute of Ferrous Technology, Pohang University of Science and Technology. Contact e-mail: cslee@postech.ac.kr

Manuscript submitted December 22, 2011.

Article published online June 13, 2012

STS, such as surface passive film characteristics, internal hydrogen behavior, Laves phase precipitation, *etc.*, were explored, and a method to suppress these influencing factors was suggested.

## II. EXPERIMENTAL

Two kinds of ferritic STSs, 430 and 445NF, were used and their chemistry is shown in Table I: as aforementioned, 445NF STS contains higher Cr, Ti and Nb contents than 430 STS. The steels were supplied in the form of a plate with 1.5 mm thickness, which were produced in sequence of hot rolling, annealing, cold rolling, and annealing.

Hydrogen was introduced into the samples by electrochemical charging at 298 K (25 °C) in a 3 pct NaCl + 0.3 pct NH<sub>4</sub>SCN solution for 72 hours with current density ranging from 0.1 to 10 A/m<sup>2</sup>. Hydrogen charging by the electrochemical method is known to be sensitive to surface roughness, and hence, the sample surface was ground using SiC emery paper (#400 to #2000). The hydrogen content was analyzed by a thermal desorption spectrometry (TDS) with a gas chromatograph (Agilent GC 7890A; Agilent Technologies, Santa Clara, CA) with a uniform specimen size of 1 cm × 3 cm × 1.5 mm thickness. During the TDS analyses, the sample was heated from 298 K to 873 K (25 °C to 600 °C) at a heating range of 100 K/h, and the emitted gas was collected at 5-minute intervals under a continuous He gas flow. To estimate the activation energy of hydrogen detrapping, various heating rates of 50, 100, 200, and 300 K/h were also applied.

Tensile tests were carried out on the uncharged samples of Figure 1(a) using an Instron 8501 machine (Instron Corporation, Norwood, MA) at an initial strain rate of  $5 \times 10^{-3}$ /s. Hydrogen embrittlement behavior was examined by slow strain rate tests (SSRTs) and bending tests with the charged samples. The charged samples were coated with Cd by an electrochemical method in fluoroborate bath for 5 minutes at room temperature prior to SSRTs and bending tests to prevent hydrogen emission during the tests.

SSRTs were also conducted using an Instron 8501 machine at a stroke rate of 0.005 mm/min. The samples for the SSRT were notched as shown in Figure 1(b). The notch can increase the degree of stress concentration for easy fracture.<sup>[14]</sup> Hydrostatic stress generated near the notch results in high dislocation density, which subsequently increases hydrogen solubility.<sup>[9,15]</sup>

The fracture stress was defined as the maximum tensile stress, which was calculated by the maximum tensile load divided by the minimum area of the initial cross section at the notch.

**Table I. Chemical Composition of Specimens used in this Study (wt pct)**

	Cr	Ni	Mo	Cu	Ti	Nb
430 STS	16	0.27	0.03	0.08	0.002	0.002
445NF STS	21	—	—	0.4	0.3	0.1

Bending tests were conducted on the plate samples of Figure 1(c) using a metal formability analysis system at a loading rate of 60 mm/min. The bending test procedure is illustrated in Figure 2. First carried out was 90 deg bending; if there were no cracks during loading at the bent tip, the 90 deg bent samples were subsequently subjected to 180 deg folding. Occurrence of cracks at the bent tip (90 deg bending) or the folded tip (180 deg folding) during loading was regarded as degradation of formability associated with hydrogen.

The overall corrosion behavior was examined by potentiodynamic polarization tests in an aerated 3.5 pct NaCl solution at pH-neutral. The test samples were cut to appropriate size and abraded with SiC emery paper (to #2000) prior to the electrochemical examination. The reference electrode was a saturated calomel electrode ( $V_{SCE}$ ) and the counter electrode was a high-purity graphite rod. The relationship between the alloying elements and the passive film properties was examined by X-ray photoelectron spectroscopy (XPS) depth profiling.<sup>[16]</sup> XPS depth profiling was performed on an ESCA ALAB 250 (Thermo Scientific, Waltham, MA) with a 15-kV monochromatic Al source at a sputtering rate of 0.07 Å/s. The analyzed depth was up to 10 nm from the specimen surface.

## III. RESULTS

### A. Microstructures and Mechanical Properties Before Hydrogen Charging

Optical micrographs of the as-received 430 and 445NF STS specimens are shown in Figure 3. The grain

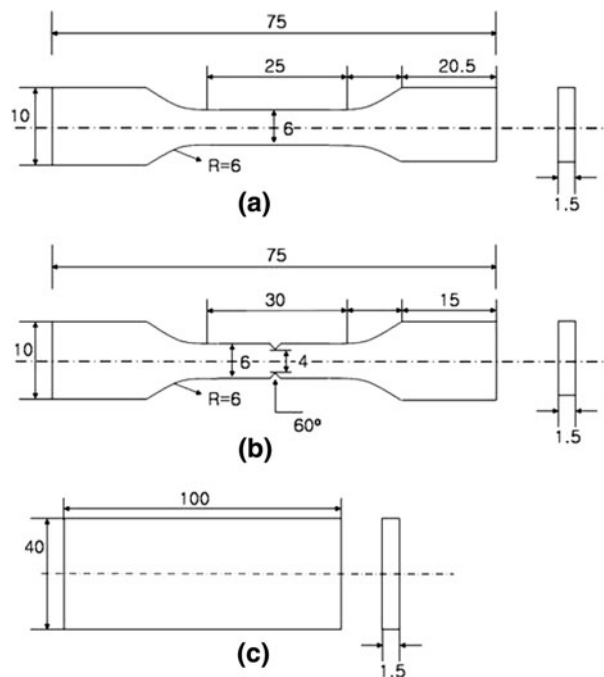


Fig. 1—Dimensions of (a) the smooth samples for tensile tests, (b) the notched samples for slow strain rate tests, and (c) the plate samples for bending tests (unit: mm).

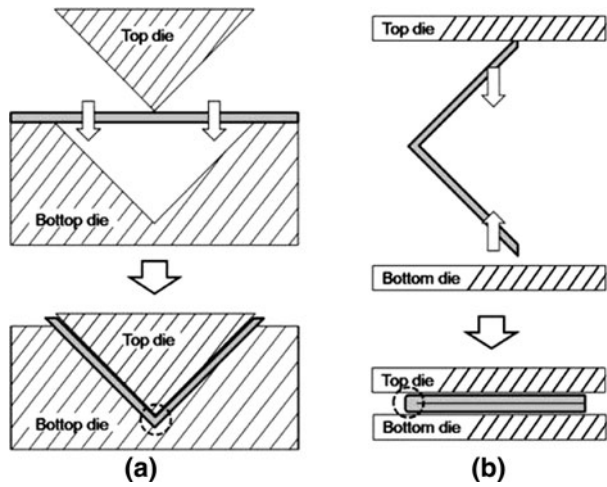


Fig. 2—Illustration showing the bending test to evaluate formability: (a) 90 deg bending and (b) 180 deg folding after 90 deg bending if there is no crack at the bent tip.

sizes were 14  $\mu\text{m}$  and 22  $\mu\text{m}$  for 430 STS and 445NF STS, respectively. Their nominal stress–strain curves are shown in Figure 4(a). 445NF STS exhibited higher yield strength and elongation but lower tensile strength than 430 STS. The higher yield strength of 445NF STS is considered because of the higher amounts of interstitial and substitutional solutes, and the lower tensile strength is caused by its lower work-hardening rate. As shown in Figure 4(b), no cracks were observed at the folded tip of both STSs even after 180 deg folding, indicating fairly good formability before hydrogen charging.

### B. Hydrogen Absorption/Desorption Behavior

Figure 5 shows the hydrogen desorption rates of the samples hydrogen charged at various current densities as a function of temperature (100 K/h heating rate). It is observed that the peak intensity increased with the current density for both STSs. However, the peak intensity of 430 STS (Figure 5(a)) was much stronger than that of 445NF STS (Figure 5(b)) at the same current density, implying that a higher concentration of hydrogen was introduced in 430 STS than in 445NF STS.

Meanwhile, both STSs revealed only one peak at approximately 373 K to 393 K (100 °C to 120 °C). It is known that the low temperature peaks are caused by the desorption of diffusible hydrogen, whereas the high-temperature peaks are caused by desorption of nondiffusible hydrogen. Diffusible hydrogen is responsible for hydrogen embrittlement.<sup>[14,17]</sup> The diffusible hydrogen trapping sites are known as grain boundaries<sup>[18]</sup> or dislocations,<sup>[19]</sup> and they have relatively low desorption activation energies of less than 60 kJ/mol. They typically emit hydrogen at temperatures lower than 473 K (200 °C). However, according to Turnbull *et al.*,<sup>[20]</sup> the hydrogen desorption temperature is dependent on the specimen thickness. The nondiffusible hydrogen trapping sites are the carbide/matrix interfaces,<sup>[21–23]</sup> the inclusion/matrix interfaces,<sup>[24,25]</sup> or voids<sup>[26]</sup> with relatively high

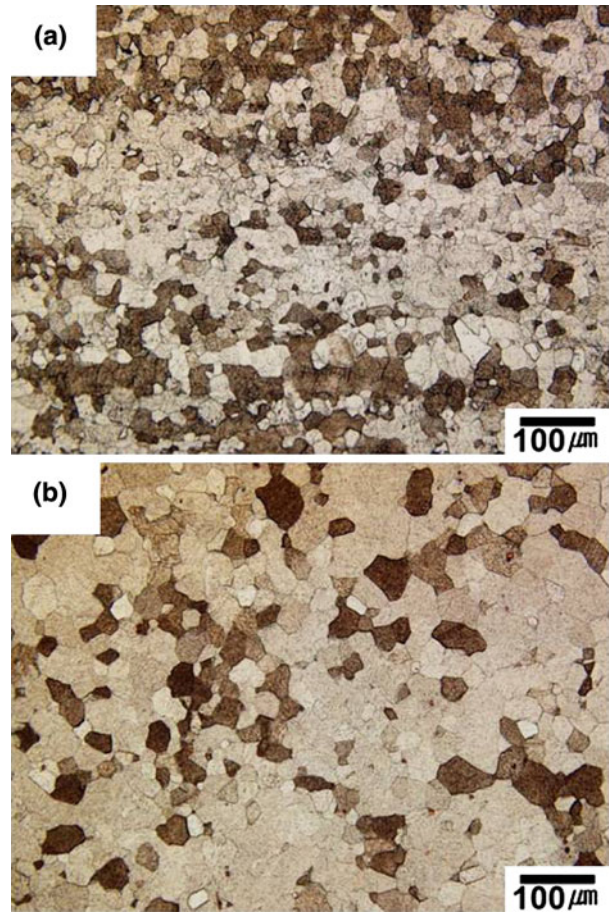


Fig. 3—Optical micrographs of the as-received STSs: (a) 430 STS and (b) 445NF STS.

desorption activation energies over 60 kJ/mol. They usually emit hydrogen at temperatures over 473 K (200 °C). To clarify the hydrogen trapping sites in 430 and 445NF STSs, the activation energy for hydrogen desorption was estimated by employing the following model proposed by Kissinger<sup>[27]</sup>:

$$\frac{\partial \ln\left(\frac{\dot{\theta}}{T_c^2}\right)}{\partial\left(\frac{1}{T_c}\right)} = -\frac{E_{aT}}{R} \quad [1]$$

where  $T_c$  is the peak temperature [K],  $\dot{\theta}$  is the heating rate [K/h],  $E_{aT}$  is the activation energy for desorption [kJ/mol], and  $R$  is the gas constant. The specimens were hydrogen charged (at uniform current density of 10 A/cm<sup>2</sup>) to measure activation energy by TDS analysis using various heating rate. The resultant Arrhenius plots of  $\ln(\dot{\theta}/T_c^2)$  vs  $(1/T_c)$  for both STSs are shown in Figure 6. The activation energies were calculated from the slope of the plot. The calculated activation energies for 430 and 445NF STSs were 19.9 kJ/mol and 18.8 kJ/mol, respectively, close to the value reported for diffusible hydrogen desorption from grain boundaries or dislocations.<sup>[18,19]</sup> Because both STSs were well annealed before hydrogen charging, it is believed that the current peak observed at 373 K to 393 K (100 °C to

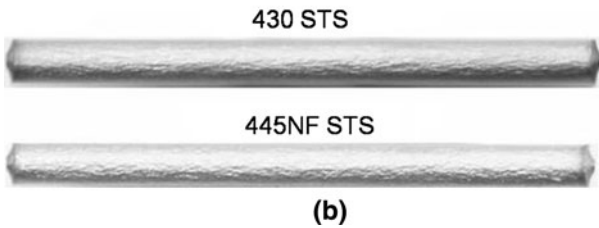
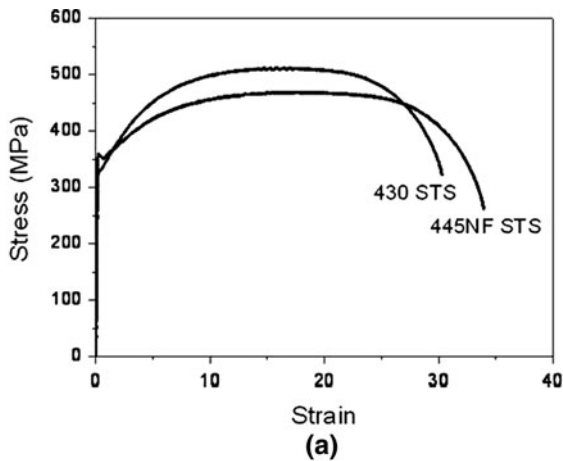


Fig. 4—(a) Nominal tensile stress–strain curves of 430 STS and 445NF STS tested at a strain rate of  $5 \times 10^{-3}$ /s before hydrogen charging. (b) Bent tip surfaces after 180 deg folding; it is noted that no cracks were observed in both 430 STS and 445NF STS before hydrogen charging even after heavy deformation.

120 °C) can be attributed to hydrogen desorption from grain boundaries.

### C. Mechanical Properties After Hydrogen Charging

First, to evaluate the effect of hydrogen on formability, two STSs charged with the same amount of hydrogen ( $\sim 0.15$  ppm) were subjected to 180 deg folding. Figure 7 shows the bent and folded tip of both STSs. Whereas 430 STS did not reveal any cracks by 180 deg folding, several large cracks were evident in 445NF STS: In the case of 445NF STS, cracking occurs even with 90 deg bending. A comparison between Figure 4(b) (bending of uncharged samples) and Figure 7 reveals that 430 STS is more resistant to hydrogen embrittlement.

Figure 8 shows the stress–displacement curves obtained from SSRTs of the samples with various hydrogen contents: Because notched samples were used, the stress–displacement curves are presented instead of the stress–strain curves. For the as-received hydrogen-free samples (sample A), elongation of 445NF STS was much larger than that of 430 STS. With increasing hydrogen content, elongation of both 430 and 445NF STSs decreased considerably. In this study, it is important to note that elongation of 445NF STS decreased at a much faster rate than that of 430 STS. For instance, for the samples containing approximately 1 ppm (sample B for 430 STS and sample D for 445NF STS), the elongation of 445NF decreased by  $\sim 70$  pct but that of 430 STS decreased by  $\sim 30$  pct compared with the uncharged specimens. This finding is in good accordance

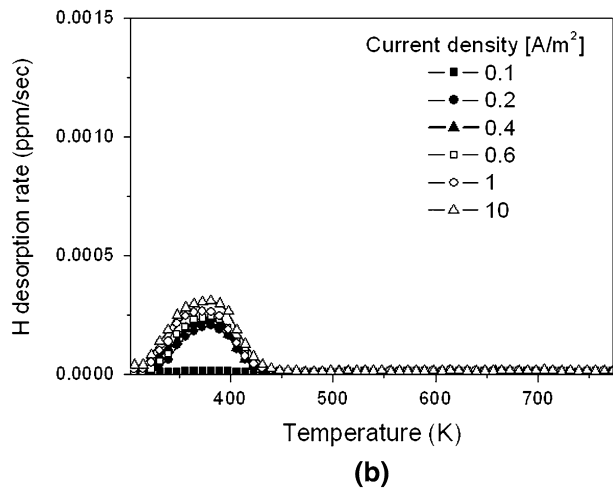
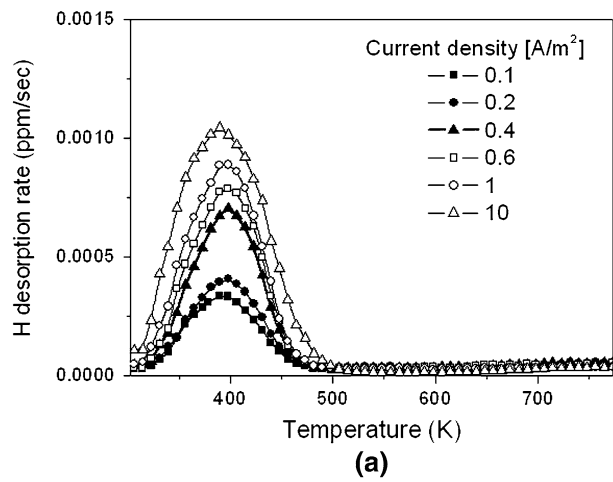


Fig. 5—Hydrogen desorption rate curves measured by a thermal desorption analysis for the samples hydrogen charged with various current densities: (a) 430 STS and (b) 445NF STS.

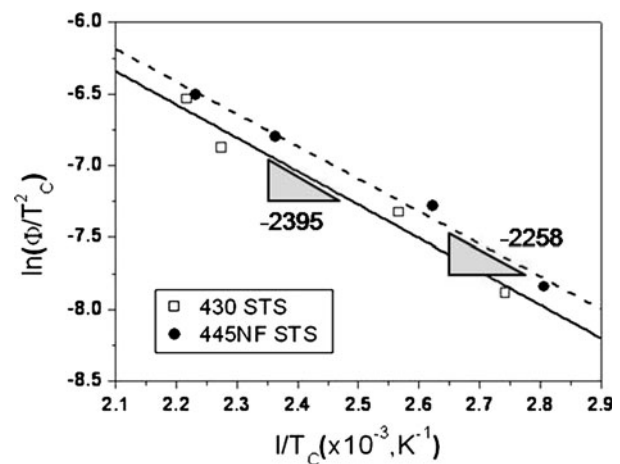


Fig. 6—Arrhenius plots of 430 STS and 445NF STS for estimating the activation energy for hydrogen desorption.

with the macroscopic pictures shown in Figure 7. From the results of Figures 7 and 8, it is clearly observed that 445NF STS is more susceptible to hydrogen embrittlement than 430 STS.

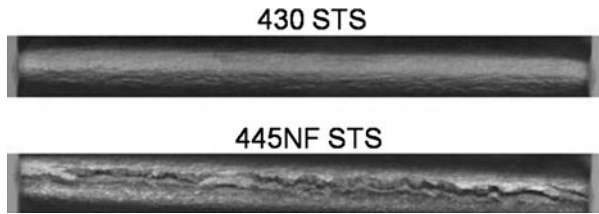


Fig. 7—Bent surfaces after 180 deg folding for 430 STS and 90 deg bending for 445NF STS containing 0.161 ppm and 0.140 ppm of hydrogen, respectively.

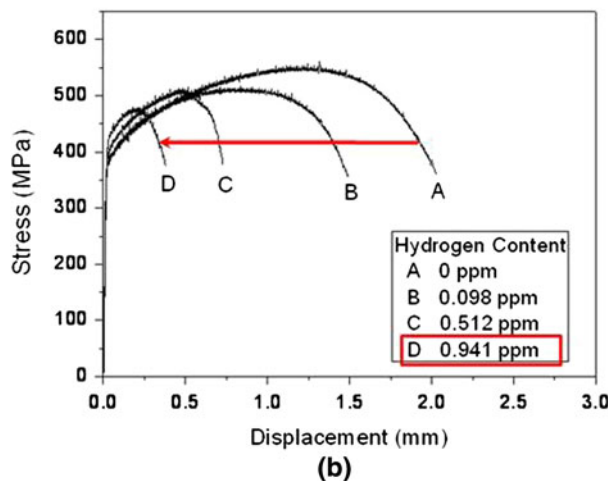
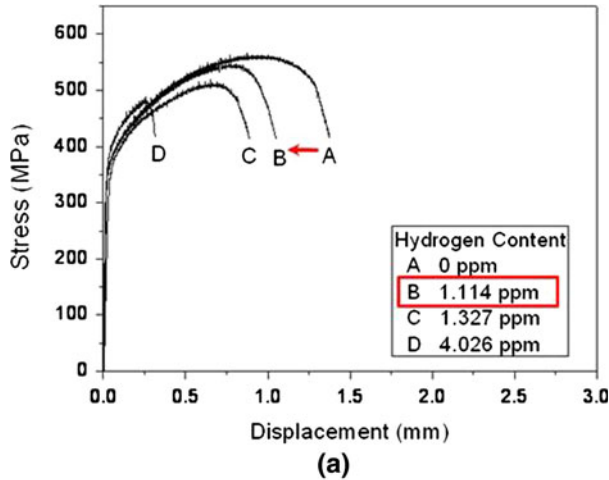


Fig. 8—Stress–displacement curves obtained from SSRTs at a stroke rate of 0.005 mm/min for (a) 430 STS and (b) 445NF STS containing the different amount of hydrogen.

#### IV. DISCUSSION

In the current study, hydrogen embrittlement behavior of 445NF STS, a newly developed ferritic STS, was (1) characterized by performing a series of hydrogen charging and mechanical tests of SSRTs and bending tests, and (2) compared with that of conventional 430 ferritic STS. As described in the preceding sections, although the hydrogen content of 445NF STS was lower than that of 430 STS under identical hydrogen charging conditions, the resistance to hydrogen embrittlement of

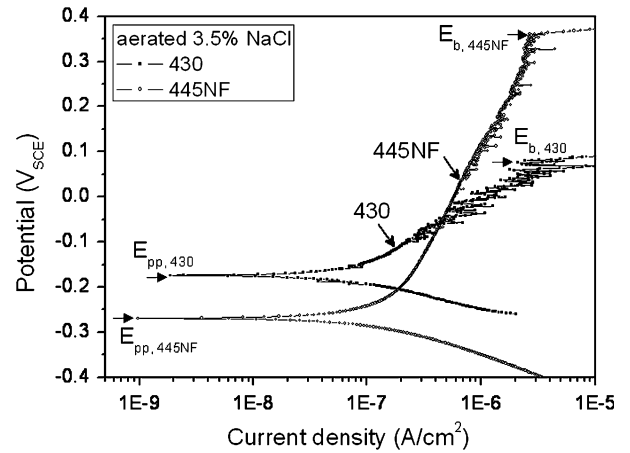


Fig. 9—Potentiodynamic polarization curves of 430 STS and 445NF STS (3.5 pct aerated NaCl solution).

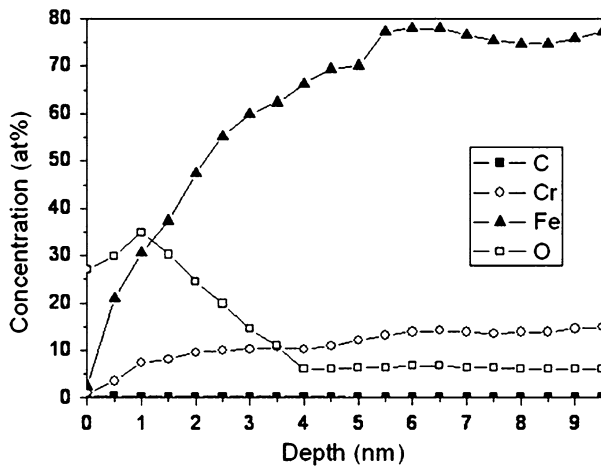
445NF STS was inferior to that of 430 STS. This contradictory result is rationalized in this section.

##### A. Effects of Passive Film on Hydrogen Absorption

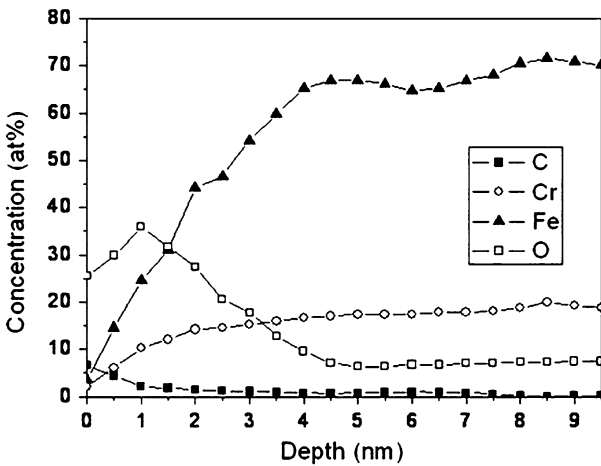
As shown in Figure 5, 445NF STS absorbed less hydrogen content than 430 STS under identical hydrogen charging conditions. Yu and Perng<sup>[7]</sup> studied the effects of the surface passive layer on the hydrogen absorption of stainless steels in a corrosive environment. Their results showed that the passive layer prevents hydrogen absorption. Similarly, Adams *et al.*<sup>[28]</sup> found that hydrogen absorption was affected by the formation of an oxide layer. Figure 9 presents the potentiodynamic polarization curves of 430 and 445NF STSs tested in a 3.5 pct aerated NaCl solution. The passive range begins at the primary passive potential ( $E_{pp}$ ), which corresponds to the start of the passive layer formation. It is also limited by the pitting potential ( $E_b$ ), which corresponds to the breakdown of the passive layer. In the current case, the passive range of 430 STS (−0.17 to 0.07 V) was narrower than that of 445NF STS (−0.27 to 0.36 V). It is thought that the higher Cr content in 445NF STS promotes the formation of a higher quality (*i.e.*, dense and stable) passive layer on the surface and it effectively prevents hydrogen absorption.

The XPS depth profiles of the passive layer on the surface of both STSs are shown in Figure 10. The effective passive layer thickness is defined as the distance from the surface to where the Cr and O content reach bulk concentrations.<sup>[29]</sup> The measured effective passive layer thickness of 430 and 445NF STSs was approximately 4.1 nm and 5 nm, respectively.

Figure 11 presents the spectra of oxide and metallic components at 1 nm depth from the surface. The components of the passive layer were identified by comparing the deconvoluted peak of each component with the reference data: Cr metal (binding energy: 574.4 eV),  $Cr_2O_3$  (576.0–576.1 eV),  $Cr(OH)_3$  (577.2 eV), and  $Cr_2(SO_4)_3$  (578.3 eV). Among the oxide film components,  $Cr_2O_3$  is higher in 445NF (~30 pct) than in 430 (~13 pct). It is generally accepted that the presence



(a)



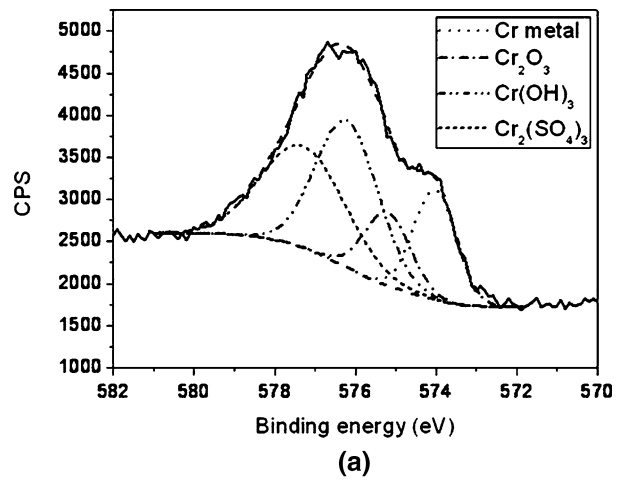
(b)

Fig. 10—XPS profile showing the atomic concentration variation with depth from the surface: (a) 430 STS and (b) 445NF STS.

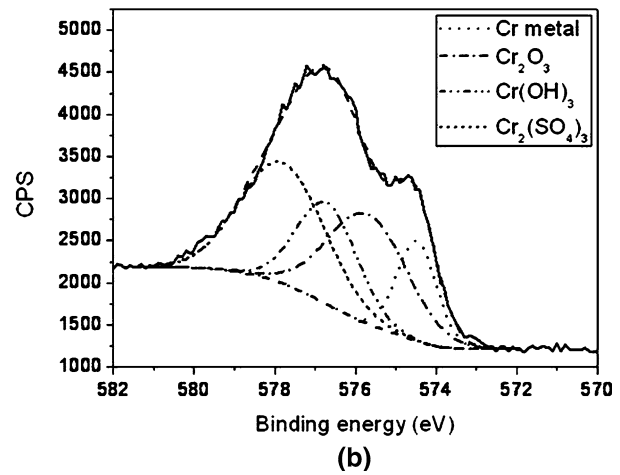
of a passive film could pose a barrier for hydrogen introduction.<sup>[30–32]</sup> One effective parameter for promoting hydrogen permeation is the diffusivity of hydrogen in  $\text{Cr}_2\text{O}_3$ . The hydrogen diffusivity of  $\text{Cr}_2\text{O}_3$  ( $9.2 \times 10^{-16} \text{ cm}^2/\text{s}$ )<sup>[33]</sup> is much lower than that of the bcc lattice ( $1.0$  to  $1.3 \times 10^{-7} \text{ cm}^2/\text{s}$ )<sup>[7]</sup> at room temperature. As shown in Figure 11,  $\text{Cr}_2\text{O}_3$  component in a passive film of 445NF STS is twofold greater in quantity compared with that in of 430. As a result, hydrogen introduction in 445NF STS would be more difficult than in 430 STS because of the formation of a thicker stable passive film and a greater portion of the  $\text{Cr}_2\text{O}_3$  in the passive film.

### B. Degradation of Mechanical Properties by Hydrogen

The degradation of mechanical properties after hydrogen charging inferred from Figure 8 is shown in Figure 12 as a function of diffusible hydrogen. The measurement method for diffusible hydrogen is described in detail in Section III–B. Degradation of the notched fracture strength of 445NF STS with the hydrogen content was more severe than that of 430 STS (Figure 12(a)). The notched fracture strength decreased at a rate of  $\sim 20 \text{ MPa/ppm[H]}$  for 430 STS compared



(a)



(b)

Fig. 11—XPS spectra of Cr as a component of various layers in the passive film (solid line: experimental, dash line: deconvoluted results): (a) 430 STS and (b) 445NF STS.

with a rate of  $\sim 63 \text{ MPa/ppm[H]}$  for 445NF STS. Degradation of the displacement at final fracture (equivalent to fracture elongation in a normal tensile test) showed a similar trend (Figure 12(b)). That is, the displacement of 430 STS degraded at a rate of  $\sim 0.3 \text{ mm/ppm[H]}$ , whereas that of 445NF STS decreased at a rate of  $\sim 1.9 \text{ mm/ppm[H]}$ . This analysis again clearly revealed that 445NF STS is more susceptible to hydrogen embrittlement than 430 STS.

The typical fracture surfaces of 430 and 445NF STSs hydrogen-charged at  $0.2 \text{ A/m}^2$  for 72 hours are shown in Figure 13: After such hydrogen charging, 430 and 445NF STSs contained 1.3 ppm and 0.5 ppm hydrogen, respectively. The fracture surface of 430 STS with 1.3 ppm hydrogen (Figure 13(a)) shows a partially ductile fracture surface with dimples and a partially faceted fracture surface. In the case of 445NF STS, ductile fracture with dimples occurred without hydrogen charging (Figure 13(b)), but the ratio of faceted fracture to ductile fracture increased with increasing degree of embrittlement and inclusion fracture after hydrogen charging of 0.5 ppm (Figure 13(c)).<sup>[31,34]</sup> This again lends support to the finding that 445NF is more susceptible to hydrogen even with a small amount of

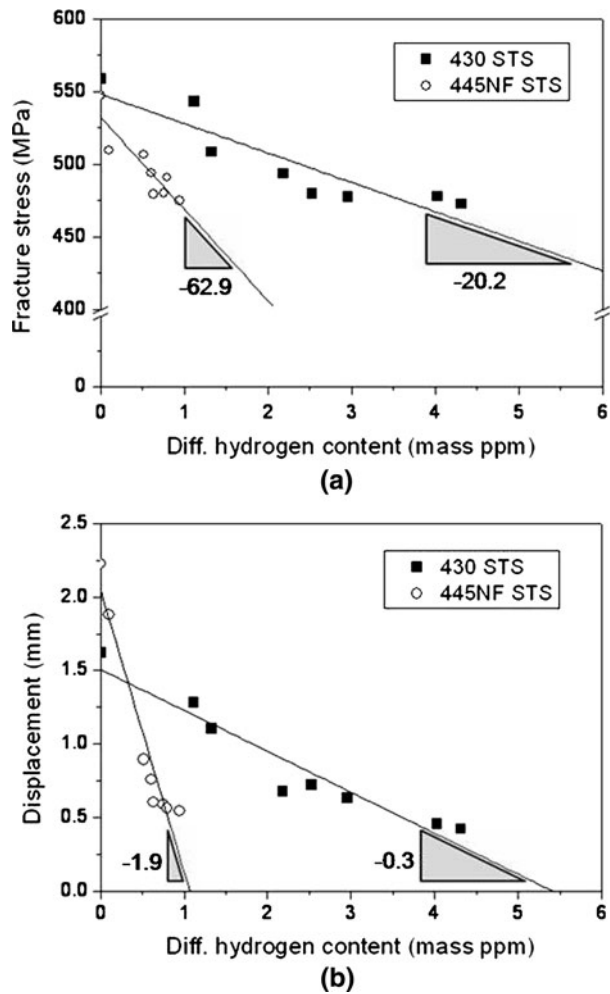


Fig. 12—(a) Reduction of fracture strength and (b) reduction of displacement by absorbed hydrogen in 430 and 445NF STS.

it. A close inspection of Figure 13(c) reveals the traces of crack initiation and propagation from small particles (indicated by arrows) at grain boundaries. Several mechanisms have been proposed to explain hydrogen embrittlement behavior in steels.<sup>[9–12]</sup> However, it is not clearly identified what mechanism governs in the current study, which needs additional investigation.

The EDS analysis of such particles (Table II) indicates that the particles are Laves phase, which contains a high concentration of Nb. The Laves phase ( $\text{Fe}_2\text{Nb}$ ) is precipitated by the addition of Nb after exposure to a temperature range of 873 K to 1123 K (600 °C to 850 °C), and it causes decrement of both ductility and toughness.<sup>[35–38]</sup> It is, hence, anticipated that the Laves phase particles were formed at the grain boundaries during annealing after cold rolling, and hydrogen trapped Laves phase/grain boundary interfaces play a role in ductility loss.

### C. Effects of the Laves Phase on Hydrogen Embrittlement

To examine the effects of the Laves phase on hydrogen embrittlement, the as-received 445NF STS

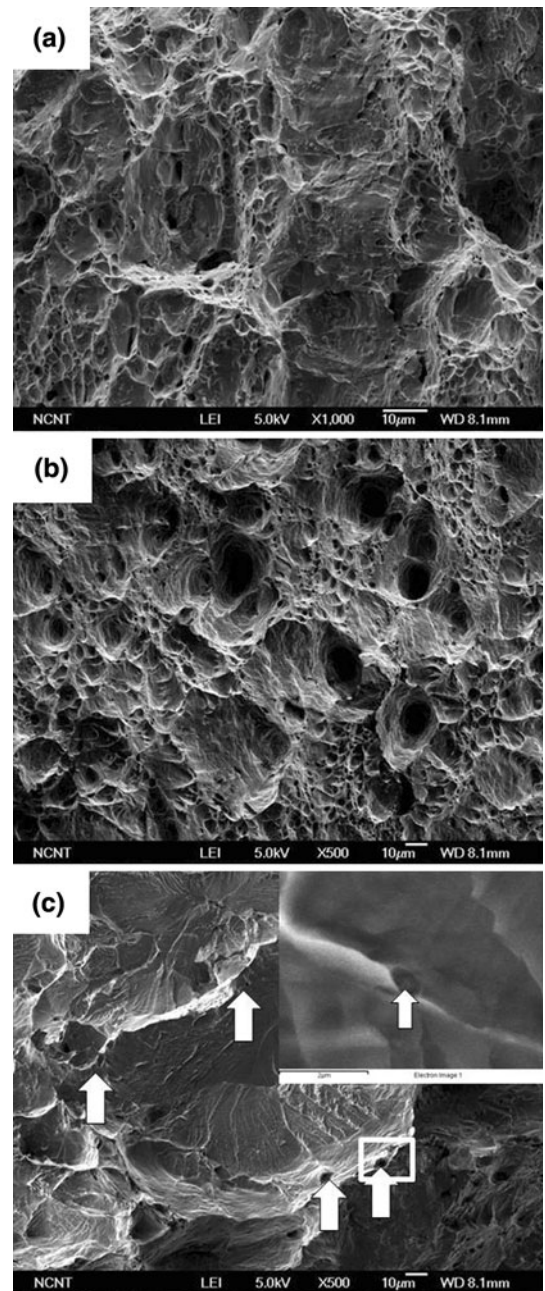


Fig. 13—Fractography of the SSRTs samples: (a) 430 STS with the hydrogen content of 1.3 ppm, (b) 445NF STS before hydrogen charging, and (c) 445NF STS with the hydrogen content of 0.5 ppm. The inset is an enlarged Laves phase particle at grain boundaries.

Table II. Chemical Composition of a Particle Located Near the Fracture Origin in Fig. 13(c) (wt pct)

C	Cr	Fe	Nb
1.3	19.8	53.5	25.28

was subjected to 50 pct cold rolling ( $t \approx 0.75$  mm) and subsequent annealing at 1273 K (1000 °C) for 3 minutes. As shown in Figure 14, the microstructure

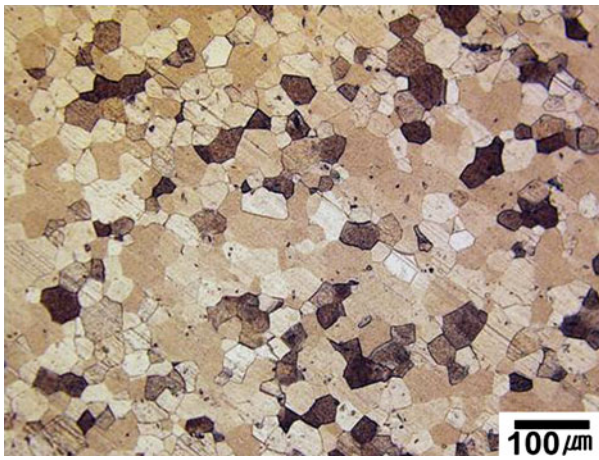


Fig. 14—Optical micrograph of 445NF STS after 50 pct cold rolling followed by annealing at 1273 K (1000 °C) for 3 min.

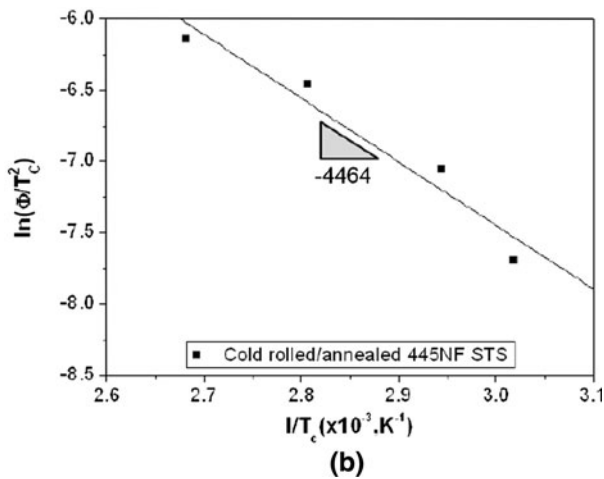
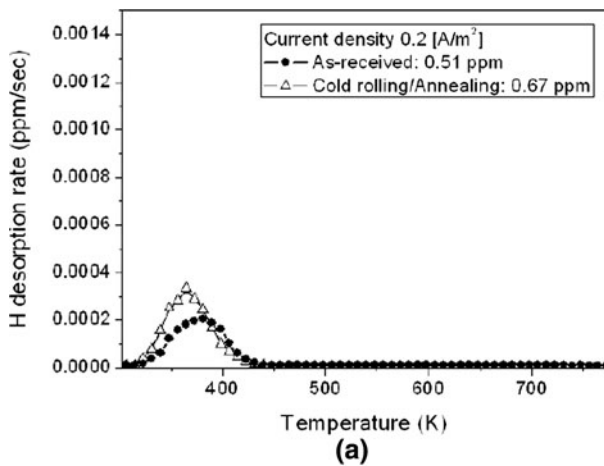


Fig. 15—(a) Hydrogen desorption rate curves of the as-received and the cold-rolled/annealed specimens, measured by a thermal desorption analysis of hydrogen charged 445NF STS at current density of 0.2 A/m<sup>2</sup> for 72 h. (b) Arrhenius plots of cold-rolled/annealed 445NF STS for estimating the activation energy for hydrogen desorption. The calculated activation energy is 37.1 kJ/mol.

consisted of fully recrystallized grains. The grain size (~27 μm) was slightly larger than that of the as-received case (~22 μm). After annealing, the Laves phase

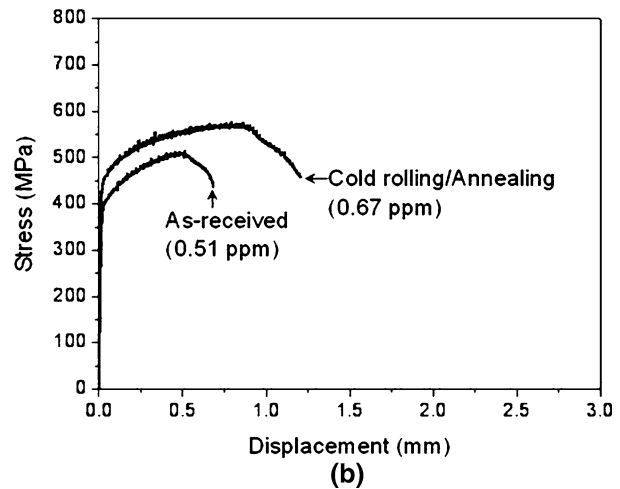
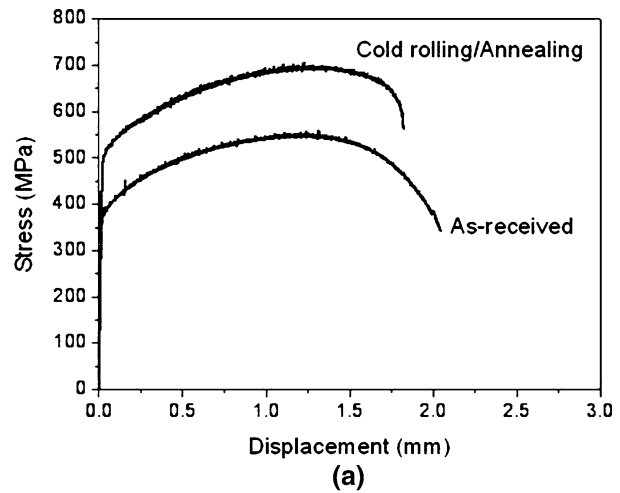


Fig. 16—SSRT results of the as-received and the cold-rolled/annealed 445NF STS: (a) without hydrogen charging and (b) after hydrogen charging.

particles were not detected by scanning electron microscopy observation.

In Figure 15(a), the hydrogen desorption rates of the as-received 445NF STS and a cold-rolled/annealed specimen hydrogen charged at 0.2 A/m<sup>2</sup> for 72 hours are compared as a function of temperature (100 K/h heating rate). The peak temperature of both the as-received and cold-rolled/annealed samples was almost the same at ~373 K (100 °C). The introduced hydrogen content of the cold-rolled/annealed 445NF STS (~0.67 ppm) was similar to that of the as-received specimen (~0.5 ppm). The resultant Arrhenius plots of  $\ln(\theta/T_c^2)$  vs  $(1/T_c)$  for cold-rolled/annealed 445NF STS is shown in Figure 15(b). The uniform current density for hydrogen charging was 10 A/cm<sup>2</sup>. The calculated activation energy was 37.1 kJ/mol, which is much higher than that of the as-received specimen (18.8 kJ/mol). Because internal hydrogen behavior is affected by distribution of alloying elements in matrix,<sup>[39,40]</sup> dissolution of Laves phases may increase activation energy for hydrogen desorption.

The SSRT results of samples without and after hydrogen charging are shown in Figure 16. In the



absence of hydrogen charging (Figure 16(a)), the cold-rolled/annealed 445NF STS exhibited higher strength and lower displacement than those of the as-received specimen. It is thought that the Laves phase dissolved by annealing at 1273 K (1000 °C), and then solid-solution hardening, particularly by Nb, occurred. After hydrogen charging, the fracture strength and ductility decreased in both samples (Figure 16(b)), but the degree of decrement was much less in the cold-rolled/annealed samples.

This indicates that the removal of the Laves phase by cold rolling/annealing increases the hydrogen activation energy and improves the resistance to hydrogen embrittlement. In other words, the Laves phase that forms at grain boundaries in a temperature range of 873 K to 1123 K (600 °C to 850 °C) is harmful because it acts as a critical diffusible hydrogen trapping site.

## V. CONCLUSIONS

Hydrogen embrittlement properties of two kinds of ferritic stainless steels, 430 STS and 445NF STS, were investigated by means of a series of hydrogen charging, slow strain rate tests, bending tests, and thermal desorption analyses. The following conclusions are drawn from the current work:

1. Under identical hydrogen charging conditions, the absorbed hydrogen content in 445NF STS was much lower than that in 430 STS. This was attributed to the formation of a thicker and more stable passive film in 445NF STS because of its higher Cr content. In addition, 445NF STS has a larger passive range in its potentiodynamic polarization curve, indicating superior corrosion resistance to 430 STS.
2. By contrast, the mechanical tests on hydrogen charged samples revealed that 445NF STS was more susceptible to hydrogen embrittlement than 430 STS. This is closely related to the Laves phase precipitation at grain boundaries of 445NF STS during annealing at 873 K to 1123 K (600 °C to 850 °C). The Laves phase particles provided crack initiation sites in association with diffusible hydrogen trapping.
3. Hydrogen embrittlement resistance as well as notched tensile strength of 445NF STS was improved by proper annealing treatment, which dissolved the Laves phase particles.

## ACKNOWLEDGMENTS

The authors are thankful for the financial support from POSCO, Korea.

## REFERENCES

1. K.H. Lo, C.H. Shek, and J.K.L. Lai: *Mater. Sci. Eng. R-Reports*, 2009, vol. 65, pp. 39–104.

2. N.R. Baddoo: *J. Constr. Steel Res.*, 2008, vol. 64, pp. 1199–1206.
3. Y.H. Lee, H. Lee, Y.I. Kim, and S.H. Nahm: *Metall. Mater. Int.*, 2011, vol. 17, pp. 389–95.
4. L. Zhang, M. Wen, M. Imade, S. Fukuyama, and K. Yokogawa: *Acta Mater.*, 2008, vol. 56, pp. 3414–21.
5. S. Singh and C. Altstetter: *Metall. Trans. A*, 1982, vol. 13A, pp. 1799–1808.
6. J.O. Ham, B.G. Kim, and S.H. Lee: *Kor. J. Metall. Mater.*, 2011, vol. 49, pp. 1–8.
7. C.L. Yu and T.P. Perng: *Acta Metall. Mater.*, 1991, vol. 39, pp. 1091–99.
8. M. Wang, E. Akiyama, and K. Tsuzaki: *Scripta Mater.*, 2005, vol. 52, pp. 403–08.
9. J. Hirth: *Metall. Trans. A*, 1980, vol. 11A, pp. 861–90.
10. H.K. Birnbaum and P. Sofronis: *Mater. Sci. Eng. A*, 1994, vol. 176, pp. 191–202.
11. M. Nagumo: *ISIJ Int.*, 2001, vol. 41, pp. 590–98.
12. H.G. Kim, I.H. Kim, S.Y. Park, J.Y. Park, and Y.H. Jeong: *Kor. J. Metall. Mater.*, 2010, vol. 48, pp. 717–23.
13. A. Szummer, E. Jezierska, and K. Lublinska: *J. Alloys Compd.*, 1999, vol. 293, pp. 356–60.
14. K.H. So, J.S. Kim, Y.S. Chun, K.-T. Park, Y.K. Lee, and C.S. Lee: *ISIJ Int.*, 2009, vol. 49, pp. 1952–59.
15. J. Lufrano and P. Sofronis: *Acta Mater.*, 1998, vol. 46, pp. 1519–26.
16. W.S. Ji, Y.W. Jang, and J.G. Kim: *Metall. Mater. Int.*, 2011, vol. 17, pp. 463–70.
17. K. Takai and R. Watanuki: *ISIJ Int.*, 2003, vol. 43, pp. 520–26.
18. W.Y. Choo and J.Y. Lee: *Metall. Trans. A*, 1982, vol. 13A, pp. 135–40.
19. M. Nagumo, K. Takai, and N. Okuda: *J. Alloys Compd.*, 1999, vols. 293–295, pp. 310–16.
20. A. Turnbull, R.B. Hutchings, and D.H. Ferriss: *Mater. Sci. Eng. A*, 1997, vol. 238, pp. 317–28.
21. S. Hinotani, Y. Ohmori, and F. Terasaki: *Mater. Sci. Eng.*, 1985, vol. 76, pp. 57–69.
22. F.-G. Wei, T. Hara, T. Tsuchida, and K. Tsuzaki: *ISIJ Int.*, 2003, vol. 43, pp. 539–47.
23. F. Wei and K. Tsuzaki: *Metall. Mater. Trans. A*, 2006, vol. 37A, pp. 331–53.
24. J.L. Lee and J.Y. Lee: *Metall. Trans. A*, 1986, vol. 17A, pp. 2183–86.
25. T. Tsuchida, T. Hara, and K. Tsuzaki: *Tetsu-to-Hagané*, 2002, vol. 88, pp. 771–78.
26. G.M. Evans and E.C. Rollason: *J. Iron Steel Inst.*, 1969, vol. 207, pp. 1591–98.
27. H.E. Kissinger: *Anal. Chem.*, 1957, vol. 29, pp. 1702–26.
28. T.M. Adams, P. Korinko, and A. Duncan: *Mater. Sci. Eng. A*, 2006, vol. 424, pp. 33–39.
29. K. Asami, K. Hashimoto, and S. Shimodaira: *Corros. Sci.*, 1978, vol. 18, pp. 151–60.
30. M.R. Louthan, Jr. and R.G. Derrick: *Metall. Trans. A*, 1975, vol. 15, pp. 565–77.
31. M.R. Louthan, Jr., G.R. Caskey, Jr., J.A. Donovan, and D.E. Rawl, Jr.: *Mater. Sci. Eng.*, 1972, vol. 10, pp. 357–68.
32. T.-P. Perng and C.J. Altstetter: *Acta Metall.*, 1988, vol. 36, pp. 1251–60.
33. M.R. Piggott and A.C. Siarkowski: *J. Iron Steel Inst.*, 1972, vol. 10, pp. 901–05.
34. M.L. Martin, I.M. Robertson, and P. Sofronis: *Acta Mater.*, 2011, vol. 59, pp. 3680–87.
35. T.F. de Andrade, A.M. Kliauga, R.L. Plaut, and A.F. Padilha: *Mater. Charact.*, 2008, vol. 59, pp. 503–07.
36. M.P. Sello and W.E. Stumpf: *Mater. Sci. Eng. A*, 2010, vol. 527, pp. 5194–5202.
37. M.P. Sello and W.E. Stumpf: *Mater. Sci. Eng. A*, 2011, vol. 528, pp. 1840–47.
38. G.M. Sim, J.C. Ahn, S.C. Hong, K.J. Lee, and K.S. Lee: *Mater. Sci. Eng. A*, 2005, vol. 396, pp. 159–65.
39. Y. Mine, K. Tachibana, and Z. Horita: *Mater. Sci. Eng. A*, 2011, vol. 528, pp. 8100–05.
40. K.I. Kim and T.W. Hong: *Kor. J. Metall. Mater.*, 2011, vol. 49, pp. 264–69.